Supplementary Information (SI) for ChemComm.
This journal is © The Royal Society of Chemistry 2025

Supporting information

An ultra-stable prelithiated Sn anode for sulfide-based all-solid-state Li batteries

Haozhe Geng,[ab] Senhe Huang,[bc] Zhenyu Zhang,*[de] Sheng Han,*[a] Rongrong Miao,[f]
Jinhui Zhu,*[b] and Xiaodong Zhuang[bc]

[a] *School of Chemical and Environmental Engineering, Shanghai Institute of Technology, Shanghai 201418, China*
Email: hansheng654321@sina.com (S. Han)

[b] *The Soft2D Lab, State Key Laboratory of Metal Matrix Composites, Shanghai Key Laboratory of Electrical Insulation and Thermal Ageing, School of Chemistry and Chemical Engineering, Shanghai Jiao Tong University, Shanghai 200240, China*
E-mail: zhujinhui1109@sjtu.edu.cn (J. Zhu)

[c] *Frontiers Science Center for Transformative Molecules, Zhang Jiang Institute for Advanced Study, Shanghai Jiao Tong University, Shanghai 201203, China*

[d] *National Engineering Research Center of Light Alloy Net Forming & State Key Laboratory of Metal Matrix Composite, Shanghai Jiao Tong University, 800 Dongchuan Road, Shanghai 200240, China*
Email: zhangzhenyu@snerdi.com.cn (Z. Zhang)

[e] *Shanghai Nuclear Engineering Research and Design Institute Co., Ltd., 169 Tianlin Road, Xuhui District, Shanghai 200030, China*

[f] *School of Chemical Engineering and Energy Technology, Dongguan University of Technology, Dongguan, 523808, China*

1. Experimental Procedures

1.1 Synthesis of sulfide solid electrolyte and electrodes

All sample preparations and treatments were conducted in an Ar-filled glove box (O_2 and H_2O < 0.1 ppm) to prevent exposure, as sulfide solid electrolytes (SSEs) are highly sensitive to oxygen and moisture. Li_6PS_5Cl (LPSC) SSE powders were synthesized following previously reported methods. A mixture of Li_2S (Sigma-Aldrich, 99.98%), P_2S_5 (Adamas, 99%), and LiCl (Adamas, 99%) was ball-milled in a ZrO_2 pot at 400 rpm for 16 hours under an Ar atmosphere. The resulting powder was pressed into pellets at 380 MPa and encapsulated in quartz vials under vacuum. These samples were then heat-treated at 480 °C for 8 hours and allowed to cool naturally. The obtained LPSC particles were further processed into fine powders via ball milling for subsequent applications.

The Li–Sn alloy (Li_xSn) anode was prepared using a mixing and pressing method. Specifically, Li powder (25 μm, China Energy Lithium Co., Ltd.) and Sn powder (50 nm, Alfa Aesar) were encapsulated in vials under an Ar atmosphere, with the addition of 10 wt% LPSC. The powders were thoroughly mixed using a vortex mixer at 800 rpm for 12 hours, followed by compression at 400 MPa for 1 minute to form the Li_xSn anode (0.9 cm in diameter). Notably, four Li_xSn anodes ($x = 0.5, 0.75, 1, 1.25$) were prepared in this study by adjusting the molar ratio (i.e., x) of Li and Sn powder. The Sn anode was prepared using the same method, but without the addition of Li powder.

The composite cathode powder was synthesized by dry ball milling a blend of $LiNbO_3$-coated single-crystal $LiNi_{0.8}Co_{0.1}Mn_{0.1}O_2$ (NCM811, Canrd Technology Co., Ltd., 70 wt%), LPSC (29 wt%), and vapor-grown carbon fiber (VGCF, Canrd Technology Co., Ltd., 1 wt%) at 360 rpm for 4 hours under an Ar atmosphere.

1.2 Characterization Methods

Cycled cells were disassembled in an Ar-filled glove box (O_2 < 0.1 ppm, H_2O < 0.1

ppm), and each component was carefully collected for subsequent characterization. To prevent air exposure, all samples were transferred using airtight gas sample holders. X-ray powder diffraction (XRD) analyses were performed on a D8 Advance X-ray diffractometer, scanning over a 2θ range of 20–80° at a rate of 6° min^{-1}. X-ray photoelectron spectroscopy (XPS) measurements were conducted on a Kratos AXIS Ultra DLD system using monochromatic Al Kα radiation (1486.6 eV), with the charge-corrected C 1s peak set to 284.8 eV. Scanning electron microscopy (SEM) was carried out on a Nova Nano SEM 450 field emission scanning electron microscope. Raman spectra were recorded using a K-Sens-532 spectrometer with a 532 nm incident laser beam.

1.3 Full cell assembly

All assembly processes were conducted in an Ar-filled glove box to maintain ultra-low oxygen ($O_2 < 0.1$ ppm) and moisture ($H_2O < 0.1$ ppm) levels. All-solid-state Li batteries (ASSLBs) were assembled using specialized cell molds, which consisted of two conductive die steel bars and a poly(ether ether ketone) (PEEK) cylinder with an internal diameter of 1 cm.

For LiSn|LiSn or Li|Li symmetric cells, 90 mg of LPSC was pressed at 360 MPa for 30 seconds to form a pellet with a diameter of 1 cm and a thickness of approximately 700 μm. LiSn or Li electrodes were then placed on both sides of the pellets to create a sandwich structure, which was inserted into the cell mold. The mass of the LiSn electrode was 9.1 mg, while the Li foil was 50 μm thick.

For full cells, the process began with pressing 90 mg of LPSC at 80 MPa for 30 seconds to form a pellet with a diameter of 1 cm and a thickness of approximately 700 μm. A composite cathode powder with various NCM811 loadings (12.7 and 38.22 mg cm^{-2}) was evenly spread on one side of the pellet, followed by pressing at 360 MPa for 30 seconds to create a two-layer pellet. Finally, an appropriate amount of LiSn (9.1 and 27.3 mg), Sn (8.6 and 25.8 mg), or Li (50 μm thick) anodes was placed on the other side of the LPSC pellet to form a sandwich structure, which was subsequently inserted into the cell mold.

1.4 Electrochemical measurements

Before starting the electrochemical tests, the assembled cell molds were subjected to a stacking pressure of 50 MPa using a digital tablet press. The working pressure was maintained by securing the cell between two steel plates bolted at each corner. All cycling procedures for the ASSLBs were conducted at room temperature (25 °C) using a Neware Battery cycler.

For the LiSn|LiSn symmetric cell, critical current density (CCD) tests were performed with current densities ranging from 0.1 to 2.0 mA cm^{-2} and a constant cycling duration of 1 hour per step. Constant-current charge/discharge cycling tests were conducted at 1 mA cm^{-2} with a capacity of 1 mAh cm^{-2}.

For full cells, constant-current charge/discharge cycling was performed within a voltage range of 2.5–4.3 V. The rate capability tests were conducted at current densities of 0.1C, 0.2C, 0.5C, 1C, and 2C, with 5 cycles at each rate. For the long-term cycling stability test, the cells were first activated at 0.1C for 5 cycles, followed by 0.5C for another 5 cycles, and subsequently cycled at 1C.

Electrochemical impedance spectroscopy (EIS) measurements were carried out using a Bio-Logic SP300 potentiostat over a frequency range of 100 kHz to 0.1 Hz with a 10-mV amplitude.

2. Ab initio molecular dynamics (AIMD) simulations

The structural optimization and AIMD calculations were conducted utilizing the Vienna ab initio simulation package (VASP) employing the projector-augmented wave (PAW) method. All computations adhered to the same generalized gradient approximation (GGA) method with the Perdew-Burke-Ernzerhof (PBE) functional for the exchange-correlation term. Electronic wave-functions were expanded in a plane-wave basis set with a kinetic energy cutoff of 500 eV. Convergence criteria for energy and forces were set at 1×10^{-5} eV and 0.01 eV $Å^{-1}$, respectively. Brillouin zone integration utilized a 3×3×3 Monkhorst-Pack k-point grid for interfacial models with large atom numbers. AIMD simulations were conducted under the NVT ensemble employing a Noséthermostat with a time step of 4 fs. Charges on various species were determined through Bader analysis.

3. Supplementary Figures

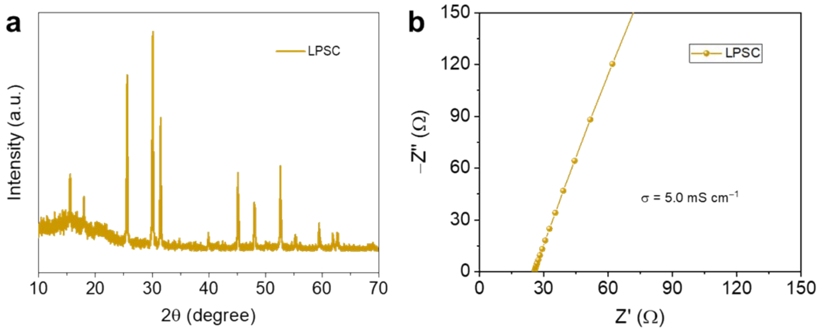

Fig. S1 XRD pattern (a) and ionic conductivity (b) of as-made LPSC SE.

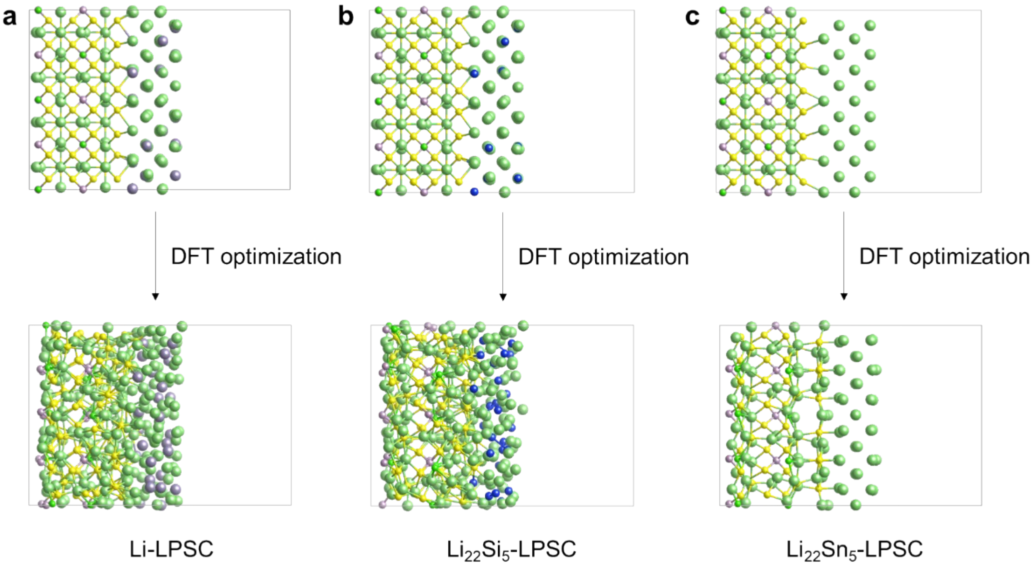

Fig. S2 Snapshots of LPSC–Li (a), LPSC–Li$_{22}$Si$_5$ (b), and LPSC–Li$_{22}$Sn$_5$ (c) interfaces before and after DFT optimization.

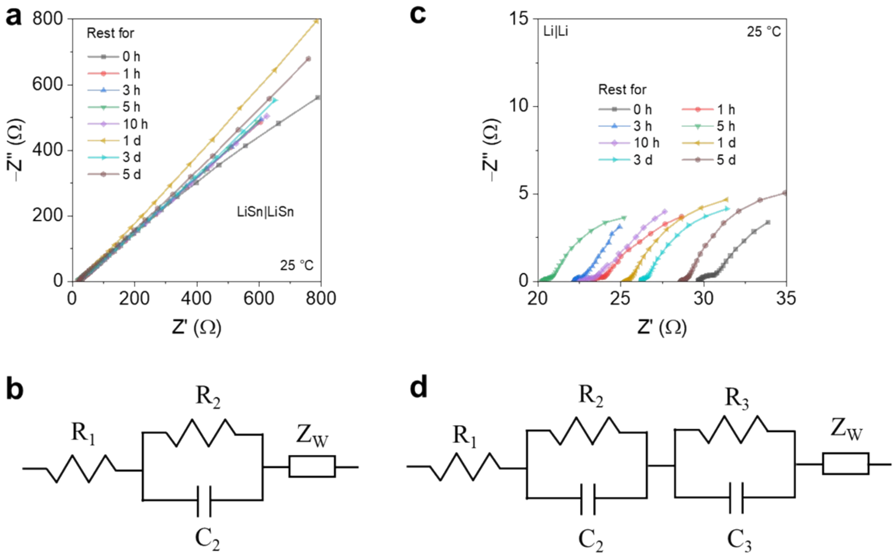

Fig. S3 Nyquist plots (a, c) and equivalent circuits (b, d) for the LiSn|LiSn and Li|Li cells, respectively, illustrating the cell's impedance with different rest times.

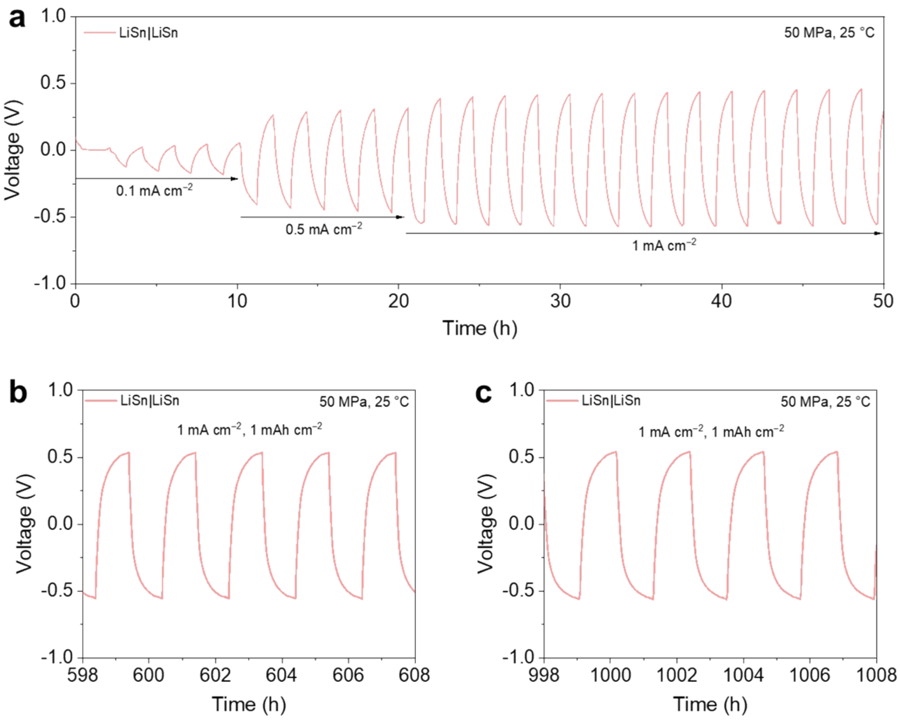

Fig. S4 Partial enlarged detail of Fig. 2a.

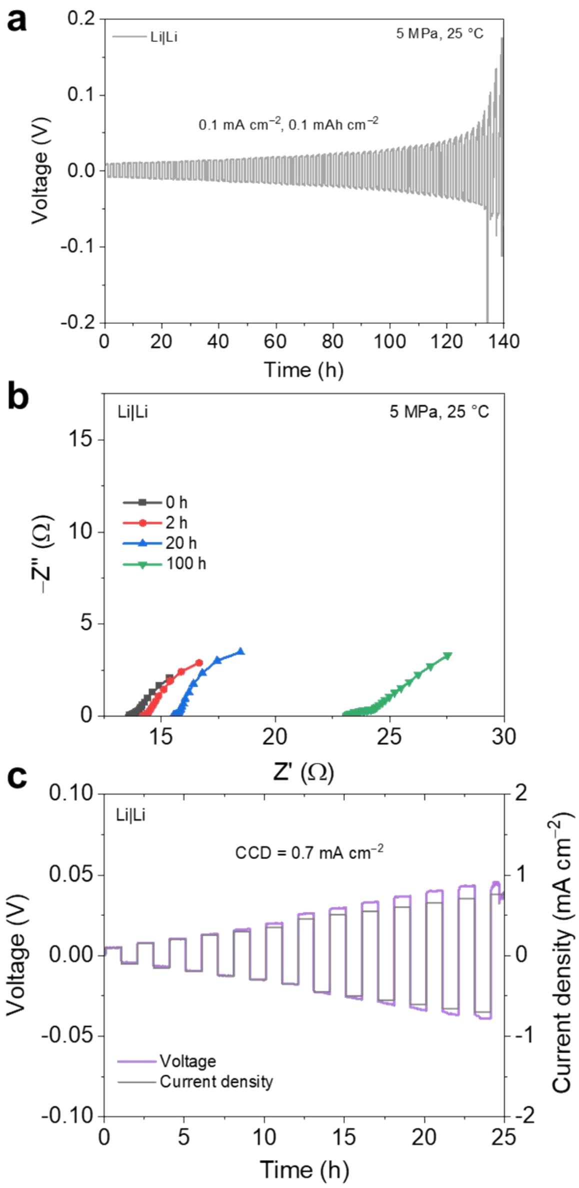

Fig. S5 (a) Discharge–charge profiles of Li|Li symmetric cells at 0.1 mA cm^{-2}, 0.1 mAh cm^{-2} at 5 MPa and 25 °C. (b) EIS spectra of Li|Li cell after cycling. (c) CCD test of Li|Li cell.

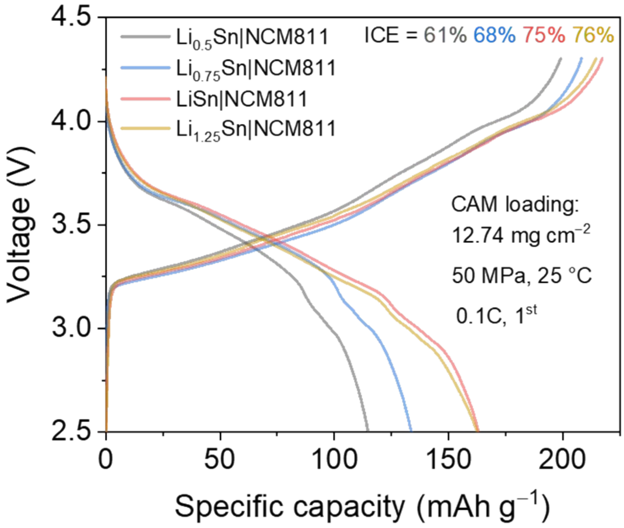

Fig. S6 Initial voltage profiles of Li_xSn|NCM811 cells with x = 0.5, 0.75, 1, and 1.25.

As shown in Fig. S6, the full cells exhibited similar performance when the anode composition varied from LiSn to $Li_{1.25}Sn$, indicating that the excess Li does not affect interfacial stability. Therefore, we selected the LiSn anode in this study, following the principle of "as little Li compensation as possible."

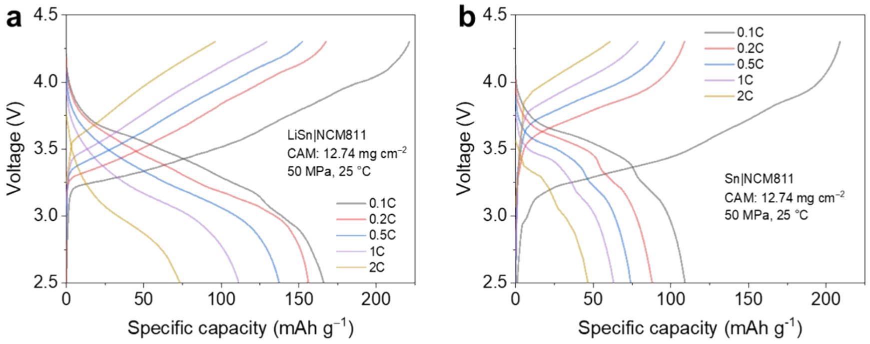

Fig. S7 Voltage profiles of LiSn|NCM811 cell (a) and Sn|NCM811 cell (b) at various rates.

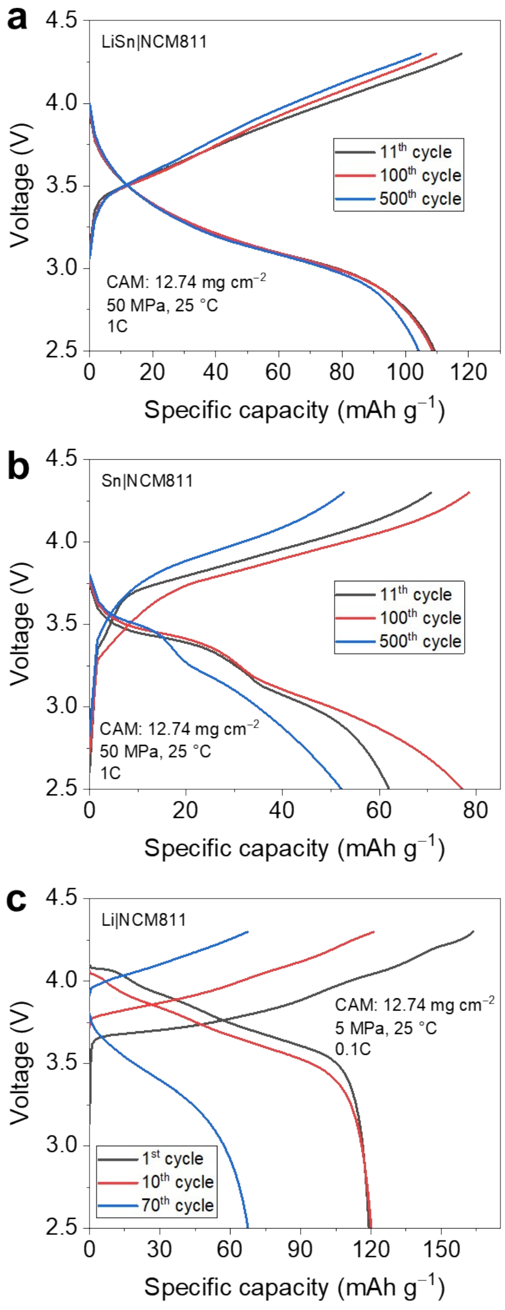

Fig. S8 Voltage profiles of LiSn|NCM811 cell (a), Sn|NCM811 cell (b), and Li|NCM811 cell (c) at different cycles.

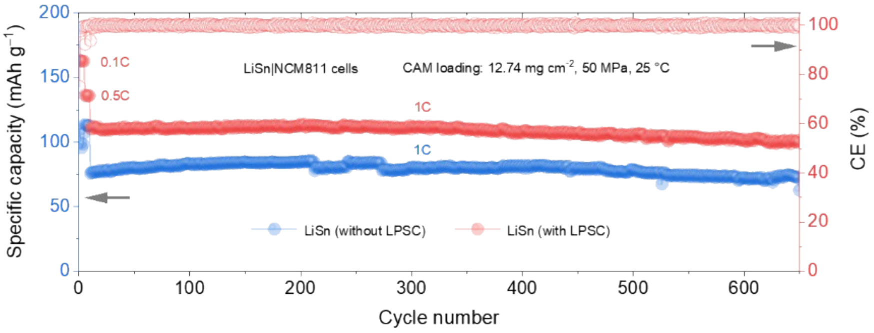

Fig. S9 Cycling performance of LiSn|NCM811 full cells, by using the anodes with and without adding LPSC electrolyte.

To assess the specific role of 10% LPSC in the anode, we prepared an LPSC-free anode and assembled the corresponding full cell for testing. As shown in Fig. S9, the LPSC-free LiSn anode-based cell exhibits a cycling performance very similar to that of the LPSC-containing anode but with a reduced specific capacity (75 vs. 112 mAh g^{-1} at 1C). This suggests that while the LiSn alloy demonstrates high stability with the LPSC electrolyte, its ionic conductivity still requires improvement.

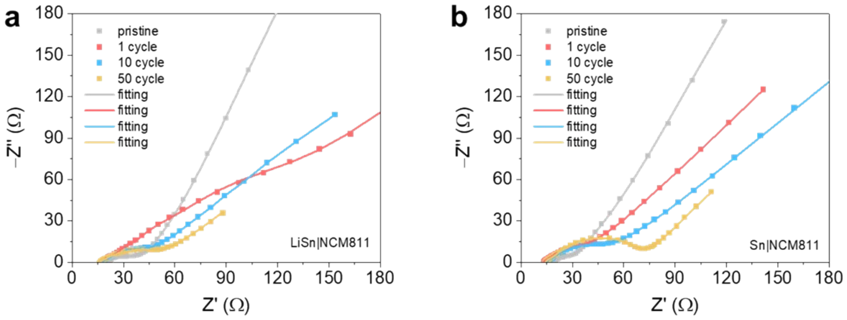

Fig. S10 Nyquist plots and corresponding fitting curves for the LiSn|NCM811 (a) and Sn|NCM811 (b) cells after different cycles.

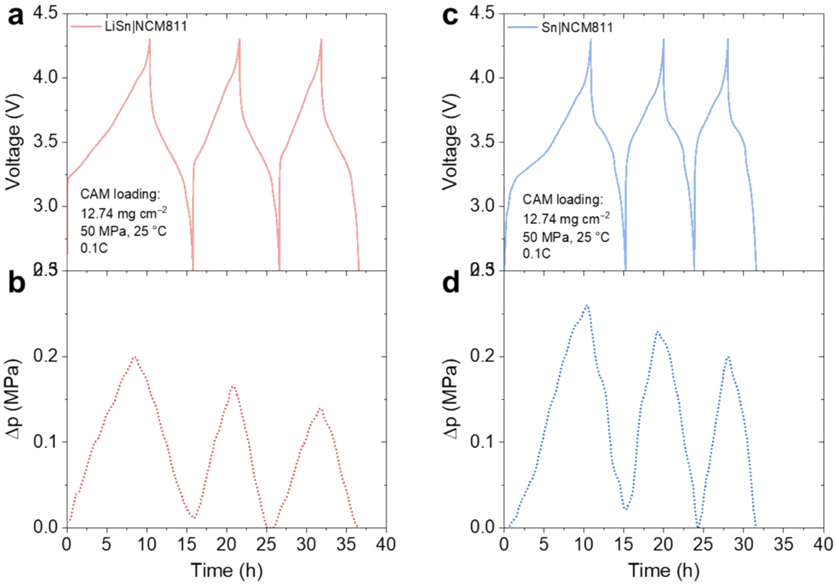

Fig. S11 Voltage profiles (a, c) and corresponding pressure change (b, d) for LiSn|NCM811 and Sn|NCM811 full cells, respectively.

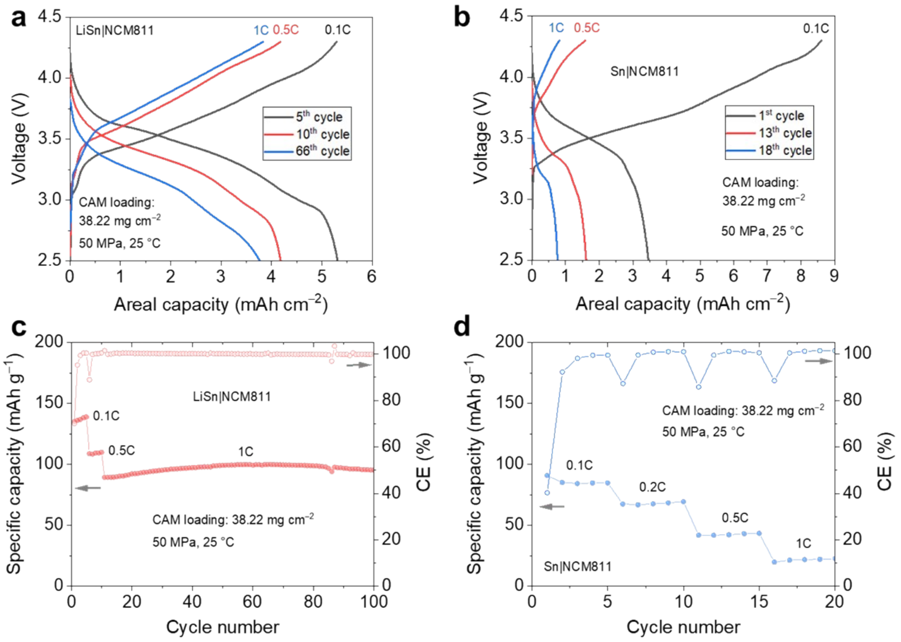

Fig. S12 Voltage profiles (a) and cycling performance (c) of LiSn|NCM811 cell under high CAM loading. Voltage profiles (b) and rate performance (d) of Sn|NCM811 cell under high CAM loading.

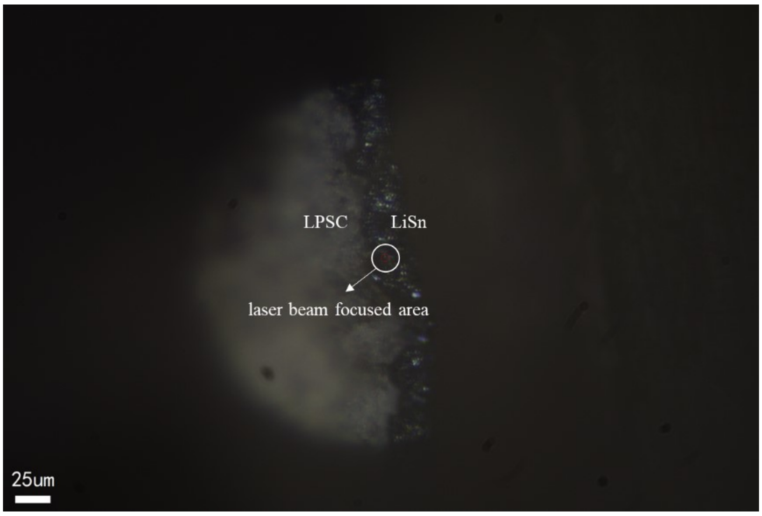

Fig. S13 Optical images of laser beam focused area in in situ Raman spectroscopy tests.

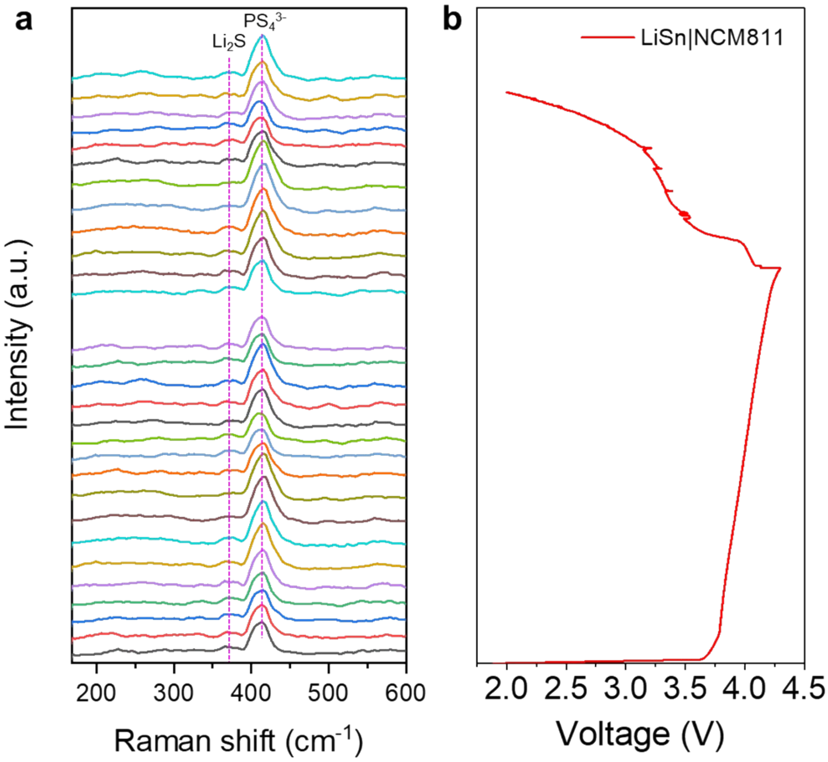

Fig. S14 (a) In situ Raman spectroscopy measurement of LiSn|NCM811 cell with laser beam focused at LiSn–LPSC interface. (b) The corresponding charging and discharging curves of the LiSn|NCM811 cell.

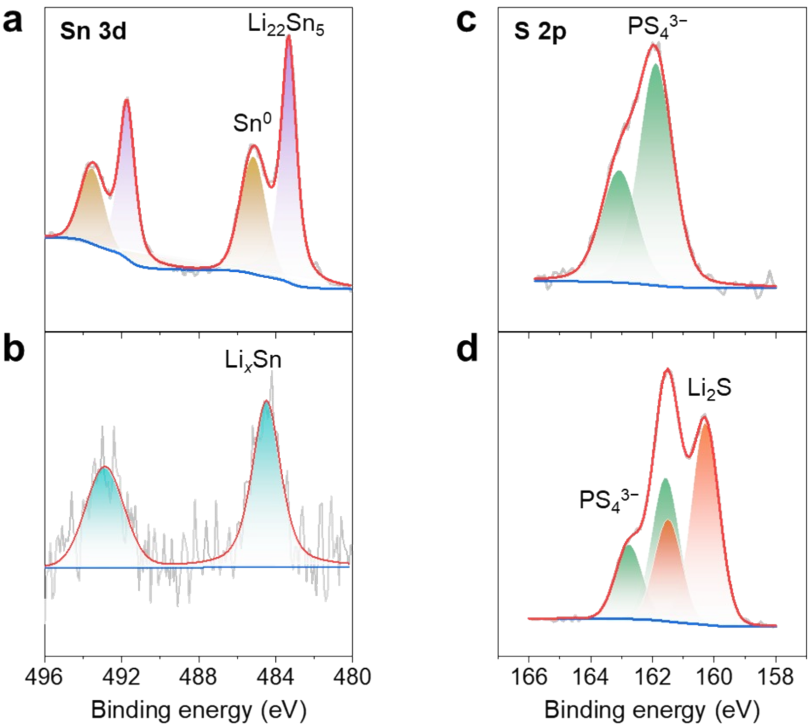

Fig. S15 Sn 3d XPS spectra of LiSn anode before (a) and after (b) cycling. S 2p XPS spectra of LiSn anode before (c) and after (d) cycling.

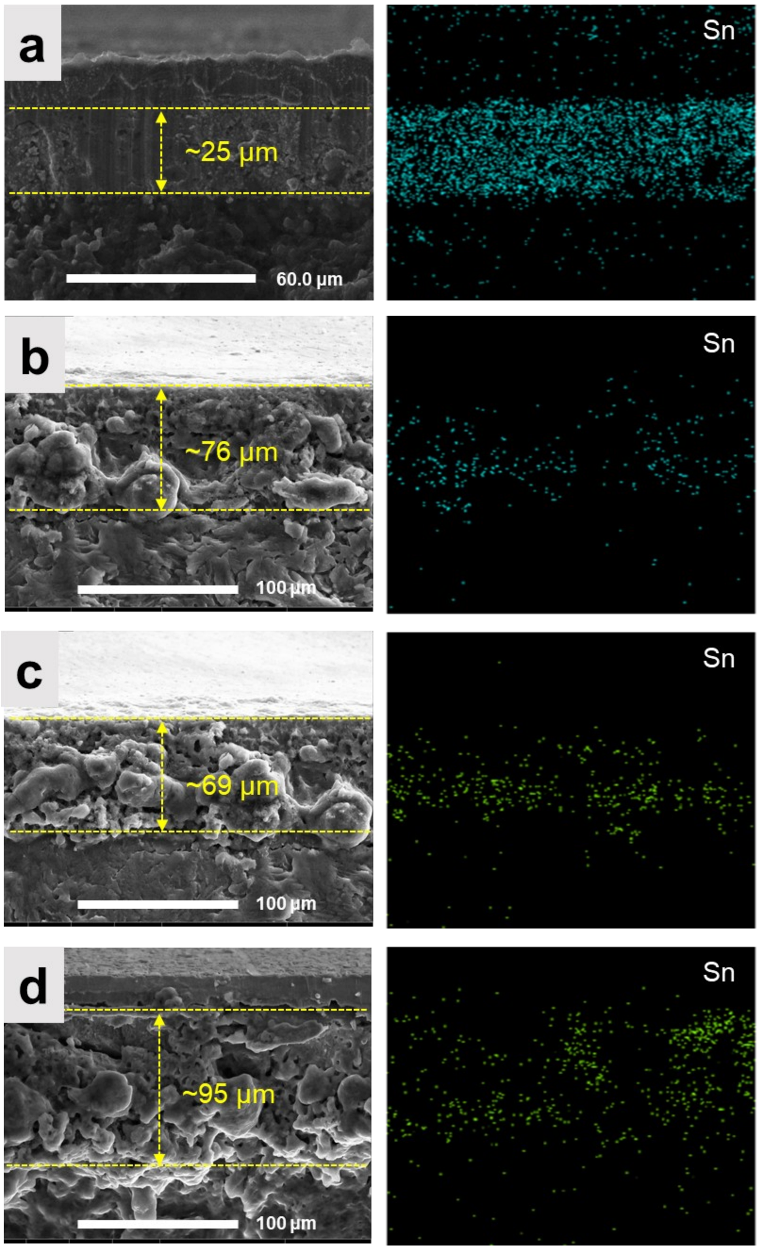

Fig. S16 The thickness of Sn anodes under the different states of fresh (a), charging (b), discharging (c), and after 50 cycles (d).

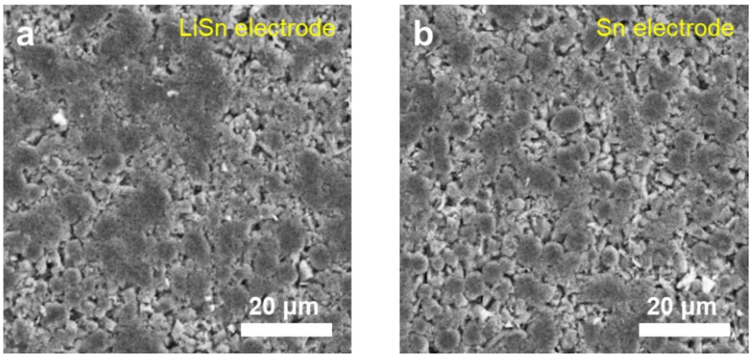

Fig. S17 Surface morphologies of LiSn anode (a) and Sn anode (b).

4. Supplementary Tables

Table S1. Fitted total resistances of LiSn|LiSn and Li|Li symmetric cells after different rest time.

Rest time	**R_t of LiSn|LiSn (Ω)**	**R_t of Li|Li (Ω)**
0 h	24.3	46.5
1 h	24.1	37.2
3 h	20.1	35.8
5 h	19.1	34.3
10 h	17.5	36.8
1 d	20.7	39.5
3 d	21.9	40.6
5 d	21.8	44.1

Table S2. Fitted resistances of LiSn|LiSn and Li|Li cells under different stages.

LiSn|LiSn cell		**Li|Li cell**	
Different stages	R_t (Ω)	Different stages	R_t (Ω)
0 h cycling	22.7	0 h cycling	13.6
2 h cycling	14.2	2 h cycling	14.2
20 h cycling	10.3	20 h cycling	15.0
200 h cycling	13.8	100 h cycling	22.3

Table S3. CCDs of symmetric cells with modified Li/Li-alloy electrodes and SSEs at 25 °C.

Anodes	**SSEs**	**Per-cycle plating capacity (mAh cm^{-2})**	**CCDs (mA cm^{-2})**	**Ref.**
Li/graphite-LPS	Li_3PS_4	1.3	1.3	[1]
Li/Li_3Bi-LiBr	$L_7P_3S_{11}$	0.84	0.84	[2]
Li/$AgNO_3$-FEC	LPSC	1.7	1.7	[3]
Li/Li-Ga alloy-LiCl	Li_3PS_4	1.5	1.5	[4]
Li/$Mg_{16}Bi_{84}$	LPSC	1.9	1.9	[5]
LiSn	**LPSC**	**2.0**	**2.0**	**This work**

Table S4. Comparison of specific capacity and cycling stability of RT sulfide ASSLBs based on reported modified LMAs, alloy and Li-alloy anodes.

Anodes	**SSEs**	**Cathodes**	**Loading (mg cm^{-2})**	**Specific capacity (mAh g^{-1}) (Rate)**	**(Capacity retention) (cycling number) (Rate)**	**Ref.**
Li/$LiAlCl_4$-LPSC	LPSC	LCO	<10	(138) (0.3C)	(~50%) (700) (1C)	[6]
Li/Li_2Te-$LiTe_3$	LPSC	NCM811	9.5	(184) (0.1C)	(95%) (400) (0.5C)	[7]
Li/$AgNO_3$-FEC	LPSC	NCM622	13.93	(167) (0.1C)	(83%) (300) (0.3C)	[3]
Li-In	LPSC	NCM622	35.67	(112) (0.53C)	(100%) (890) (0.53C)	[8]
μ-Si	LPSC	NCM811	25	(180) (0.04C)	(80%) (500) (1C)	[9]
Si composite	LPSC	NCM811	10 20	(184) (C/20) (167) (C/20)	(63%) (1000) (C/3) (72%) (650) (C/3)	[10]
Li/Al foil	LPSC	LCO	18	(122) (0.1C)	(104%) (300) (C/4)	[11]
μ-Li_xSi	LPSC	S	3	(1249) (0.05C)	(76%) (500) (0.3C)	[12]
$Li_{0.8}$Al	LGPS	S	1.07	(1362) (0.1C)	(93%) (200) (0.2C)	[13]
PL-Si	LPSC	NCM811	19.11	(187) (0.1C)	(56.8%) (300) (0.5C)	[14]
$Al_{94.5}In_{5.5}$	LPSC	NCM622	31	(159) (0.1C)	(60.9%) (100) (0.4C)	[15]
n-Si@$LiAlO_2$	LPSC	NCM83	10	(147) (0.14C)	(77%) (150) (0.5C)	[16]
LiSn	**LPSC**	**NCM811**	**12.74**	**(166) (0.1C)**	**(91%) (650) (1C)**	**This work**

Table S5. Fitted resistances of LiSn|NCM811 and Sn|NCM811 cells under different stages.

Cell stages	**LiSn|NCM811**		**Sn|NCM811**	
	R_b	**R_{int}**	**R_b**	**R_{int}**
0 cycling	20.5	17.2	18.7	15.9
1 cycling	16.7	23.6	13.1	27.7
10 cycling	17.3	30.2	14.9	39.6
50 cycling	16.1	37.7	14.3	56.6

Reference

1. X. Xing, Y. Li, S. Wang, H. Liu, Z. Wu, S. Yu, J. Holoubek, H. Zhou and P. Liu, *ACS Energy Lett.*, 2021, **6**, 1831-1838.
2. B. Zhao, Y. Shi, J. Wu, C. Xing, Y. Liu, W. Ma, X. Liu, Y. Jiang and J. Zhang, *Chem. Eng. J.*, 2022, **429**, 132411.
3. Y. Liang, C. Shen, H. Liu, C. Wang, D. Li, X. Zhao and L. Z. Fan, *Adv. Sci.*, 2023, e2300985.
4. Y. Shi, L. Hu, Q. Li, Y. Sun, Q. Duan, Y. Jiang, Y. Xu, J. Yi, B. Zhao and J. Zhang, *Energy Storage Mater.*, 2023, **63**, 103009.
5. H. Wan, Z. Wang, W. Zhang, X. He and C. Wang, *Nature*, 2023, **623**, 739-744.
6. H. Duan, C. Wang, R. Yu, W. Li, J. Fu, X. Yang, X. Lin, M. Zheng, X. Li, S. Deng, X. Hao, R. Li, J. Wang, H. Huang and X. Sun, *Adv. Energy Mater.*, 2023, **13**, 2300815.
7. H. Hao, Y. Liu, S. M. Greene, G. Yang, K. G. Naik, B. S. Vishnugopi, Y. Wang, H. Celio, A. Dolocan, W. Y. Tsai, R. Fang, J. Watt, P. P. Mukherjee, D. J. Siegel and D. Mitlin, *Adv. Energy Mater.*, 2023, **13**, 2301338.
8. S. Luo, Z. Wang, X. Li, X. Liu, H. Wang, W. Ma, L. Zhang, L. Zhu and X. Zhang, *Nat. Commun.*, 2021, **12**, 6968.
9. D. H. S. Tan, Y. T. Chen, H. Yang, W. Bao, B. Sreenarayanan, J. M. Doux, W. Li, B. Lu, S. Y. Ham, B. Sayahpour, J. Scharf, E. A. Wu, G. Deysher, H. E. Han, H. J. Hah, H. Jeong, J. B. Lee, Z. Chen and Y. S. Meng, *Science*, 2021, **373**, 1494-1499.
10. D. Cao, X. Sun, Y. Li, A. Anderson, W. Lu and H. Zhu, *Adv. Mater.*, 2022, **34**, e2200401.
11. Z. Fan, B. Ding, Z. Li, B. Hu, C. Xu, C. Xu, H. Dou and X. Zhang, *Small*, 2022, **18**, e2204037.
12. W. Ji, X. Zhang, M. Liu, T. Ding, H. Qu, D. Qiu, D. Zheng and D. Qu, *Energy Storage Mater.*, 2022, **53**, 613-620.
13. H. Pan, M. Zhang, Z. Cheng, H. Jiang, J. Yang, P. Wang, P. He and H. Zhou, *Sci. Adv.*, 2022, **8**, eabn4372.
14. Z. Fan, B. Ding, Z. Li, Z. Chang, B. Hu, C. Xu, X. Zhang, H. Dou and X. Zhang,

eTransportation, 2023, **18**, 100277.

15. Y. Liu, C. Wang, S. G. Yoon, S. Y. Han, J. A. Lewis, D. Prakash, E. J. Klein, T. Chen, D. H. Kang, D. Majumdar, R. Gopalaswamy and M. T. McDowell, *Nat. Commun.*, 2023, **14**, 3975.
16. X. Xu, Q. Sun, Y. Li, F. Ji, J. Cheng, H. Zhang, Z. Zeng, Y. Rao, H. Liu, D. Li and L. Ci, *Small*, 2023, 2302934.